RESEARCH ARTICLE

THE PROTEIN SOCIETY WILEY

Characterization of a novel format scFv×VHH single-chain biparatopic antibody against metal binding protein MtsA

Risa Asano[1] | Miyu Takeuchi[1] | Makoto Nakakido[1,2] | Sho Ito[3] | Chihiro Aikawa[4] | Takeshi Yokoyama[5,6] | Akinobu Senoo[2] | Go Ueno[7] | Satoru Nagatoishi[8] | Yoshikazu Tanaka[5,6] | Ichiro Nakagawa[9] | Kouhei Tsumoto[1,2,8,10]

[1]Department of Bioengineering, School of Engineering, The University of Tokyo, Tokyo, Japan

[2]Department of Chemistry and Biotechnology, School of Engineering, The University of Tokyo, Tokyo, Japan

[3]Rigaku Corporation ROD Single Crystal Analysis Group Application Laboratories, Tokyo, Japan

[4]Section of Applied Veterinary Sciences, Division of Veterinary Sciences, Department of Veterinary Medicine, Obihiro University of Agriculture and Veterinary Medicine, Hokkaido, Japan

[5]Graduate School of Life Sciences, Tohoku University, Miyagi, Japan

[6]The advanced center for innovations in next-generation medicine (INGEM), Tohoku University, Miyagi, Japan

[7]RIKEN SPring-8 Center, Hyogo, Japan

[8]Medical Device Development and Regulation Research Center, School of Engineering, The University of Tokyo, Tokyo, Japan

[9]Department of Microbiology, Graduate School of Medicine, Kyoto University, Kyoto, Japan

[10]The Institute of Medical Science, The University of Tokyo, Tokyo, Japan

Correspondence
Makoto Nakakido and Kouhei Tsumoto, Department of Bioengineering, School of Engineering, The University of Tokyo, Hongo 7-3-1, Bunkyo-ku, Tokyo, Japan.
Email: nakakido@g.ecc.u-tokyo.ac.jp and tsumoto@bioeng.t.u-tokyo.ac.jp

Review Editor: Aitziber L. Cortajarena

Abstract

Biparatopic antibodies (bpAbs) are engineered antibodies that bind to multiple different epitopes within the same antigens. bpAbs comprise diverse formats, including fragment-based formats, and choosing the appropriate molecular format for a desired function against a target molecule is a challenging task. Moreover, optimizing the design of constructs requires selecting appropriate antibody modalities and adjusting linker length for individual bpAbs. Therefore, it is crucial to understand the characteristics of bpAbs at the molecular level. In this study, we first obtained single-chain variable fragments and camelid heavy-chain variable domains targeting distinct epitopes of the metal binding protein MtsA and then developed a novel format single-chain bpAb connecting these fragment antibodies with various linkers. The physicochemical properties, binding activities, complex formation states with antigen, and functions of the bpAb were analyzed using multiple approaches. Notably, we found that the assembly state of the complexes was controlled by a linker and that longer linkers tended to form more compact complexes. These

observations provide detailed molecular information that should be considered in the design of bpAbs.

1 | INTRODUCTION

Bispecific antibodies are engineered antibodies that can bind to two different epitopes simultaneously. The dual targeting concept enables a variety of therapeutic and diagnostic applications (Kaplon et al., 2023; Ma et al., 2021). Among the bispecific antibodies, biparatopic antibodies (bpAbs) are artificially modified multispecific antibodies that have multiple different epitopes within the same antigen, allowing a single antibody molecule to bind to different sites of the target antigen simultaneously. Compared with monoclonal antibodies, which can only bind to single sites of an antigen, bpAbs can increase binding avidity and exhibit distinct antigen–antibody complex formation (Akiba & Tsumoto, 2020). The format of bpAbs varies widely, but they are classified into two groups: immunoglobulin G-like containing the Fc region and fragment-based without the Fc region (Brinkmann & Kontermann, 2017; Labrijn et al., 2019). Fragment-based bpAb formats can be designed relatively simply by combining antibodies into one molecule, offering efficient production with high yields and reduced costs (Brinkmann & Kontermann, 2017). These bpAb formats have the advantages of high tissue permeability (Ma et al., 2021) and easy access (Brinkmann & Kontermann, 2017; Fan et al., 2015) to the target antigen due to their smaller size compared to antibodies with the Fc region. To date, the majority of fragment-based antibodies have been developed by combining the same modality, such as tandem single-chain variable fragment (scFv) (Akiba et al., 2020; Yumura et al., 2017), tandem camelid heavy-chain variable domain (VHH) (Emmerson et al., 2011; Henry et al., 2021; Roovers et al., 2011; Walter et al., 2022), and tandem variable heavy (VH) chain (Bracken et al., 2021). Combinations of different modalities have also been developed, such as antigen binding fragment (Fab)-scFv (Lu et al., 2002) and Fab-VHH (Pekar et al., 2020). These combined formats expand options for the development of engineered antibodies (Spiess et al., 2015). However, the understanding of changes of physical properties due to the connection of different-sized antibodies remains limited, which makes it challenging to choose the appropriate molecular format for a desired function against a target molecule. Moreover, optimizing the design of constructs, including the

selection of appropriate fragment antibody modalities and adjustment of linker length for individual bpAbs, is required.

Among the various engineered antibody fragment formats, scFvs and VHHs, also known as nanobodies, are widely utilized. scFvs are minimal antibody fragments that contain a complete antigen binding site of a conventional antibody. These modules are single-chain molecules of ∼30 kDa in which two variable domains (variable heavy and variable light) are connected with a flexible linker that is typically a $(G_4S)_3$ sequence. They can be easily expressed in functional form in the *Escherichia coli* expression system (Ahmad et al., 2012). VHHs are 15 kDa single domain antibodies derived from camelid heavy chain antibodies, which typically exhibit high affinity and stability, good solubility, and a high expression level in *E. coli* (Bannas et al., 2017; Muyldermans, 2013). Both scFvs and VHHs are small-sized antibodies and high-affinity binders, but they show distinct characteristics in antigen recognition. While scFvs favor flat linear epitopes, the epitopes of VHHs are highly diverse and enable binding to cleft and pocket epitopes as well as flat ones, which are not accessible to conventional antibodies (Asaadi et al., 2021; Henry & MacKenzie, 2018). By taking advantage of these characteristics, scFvs and VHHs have been used in various therapeutic, diagnostic, and research applications (Asaadi et al., 2021).

MtsABC transporter is expressed on the cell surface of *Streptococcus pyogenes*, which causes a wide range of human infections (Brouwer et al., 2023). This transporter plays a crucial role in uptake of manganese and iron (Jakubovics, 2019). Uptake of manganese is critical for the growth of Group A Streptococcus under oxidative conditions (Turner et al., 2019). Also, iron is important for the growth and survival, but the availability of iron in the host is limited (Ge & Sun, 2014). MtsA, part of the MtsABC transporter is a lipoprotein that is connected to the outside of the cell membrane by an N-terminal lipid anchor, and it binds with free metals. Previous researchers reported that a recombinant MtsA binds not only to manganese and iron but also to zinc (Lei et al., 2003; Sun et al., 2008). The X-ray structure of iron-bound MtsA was solved at 1.8 Å resolution, which demonstrated that metal ions bind to a pocket between two N- and C-terminal lobes (Sun et al., 2009). Additionally,

the analysis of homolog proteins of MtsA revealed that they change their conformation upon metal binding from the open to the closed state (Couñago et al., 2014; de Boer et al., 2019). Restriction of the conformational change might regulate the function of MtsA and affect the acquisition of metal ions of *S. pyogenes* from the host environment.

Herein, we developed a novel single-chain fragment-based bpAb consisting of both a scFv and a VHH that is designed to inhibit metal binding of MtsA (Figure 1). Following the selection of a suitable linker based on crystal structures, we successfully expressed the designed bpAb as a recombinant protein. We then assessed the characteristics of this bpAb using a physicochemical approach. Interestingly, we revealed that the complex formation states were clearly altered by linker length. Based on our observations, we discuss the utility of the scFv–VHH asymmetric format from a molecular perspective and proposed steps for optimal future development of bpAbs.

2 | RESULTS

2.1 | Generation of scFv and VHH against MtsA

We first obtained fragment antibodies that bind to different epitopes of MtsA. To generate MtsA-specific scFvs, a
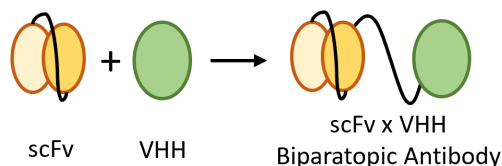
FIGURE 1 Constructs of the bpAb in this study. Schematic representation of the scFv-VHH bpAb. scFv and VHH are fused by a single amino acid linker.

rabbit was immunized with recombinant MtsA. After confirmation that the serum titer was elevated, RNA was extracted from the spleen of the rabbit and cDNA was generated by reverse transcription. Variable fragment (Fv) sequences were amplified and cloned into a phagemid vector to generate scFvs. In parallel, an alpaca was immunized to generate VHHs. cDNA was prepared by RNA extraction followed by reverse transcription. VHH sequences were amplified and incorporated into another phagemid vector. Using phage display technology, we selected scFvs and VHHs from each library. After second rounds of bio-panning, we conducted ELISA assays with immobilized MtsA, and the DNA sequences of clones showing a MtsA-specific signal were analyzed. Based on the ELISA results and the clustering of complementarity determining region (CDR) sequences, we chose scFv13 and VHH43 for further analysis.

2.2 | Binding characteristics of scFv13 and VHH43 against MtsA

We prepared scFv13 and VHH43 as recombinant proteins using the *E. coli* expression system. Since the rabbit antibody has a disulfide bond in the form of a bridge between the variable and the constant region of the kappa chains (Kawade et al., 2018), the cysteine residue becomes exposed on the surface when converted into scFv. To avoid dimerization, the cysteine on residue 238 was replaced with a serine. We employed surface plasmon resonance (SPR) and isothermal titration calorimetry (ITC) to characterize the binding of scFv13 and VHH43 to the antigen MtsA. The SPR analysis showed that scFv13 and VHH43 bound to MtsA with the dissociation constant (K_D) value of 1.0 and 27 nM, respectively (Figure 2a and Table 1). The values of the individual association (k_{on}) and dissociation (k_{off}) rate constants for scFv13 were $5.8 \times 10^5 M^{-1} s^{-1}$ and $5.7 \times 10^{-4} s^{-1}$,
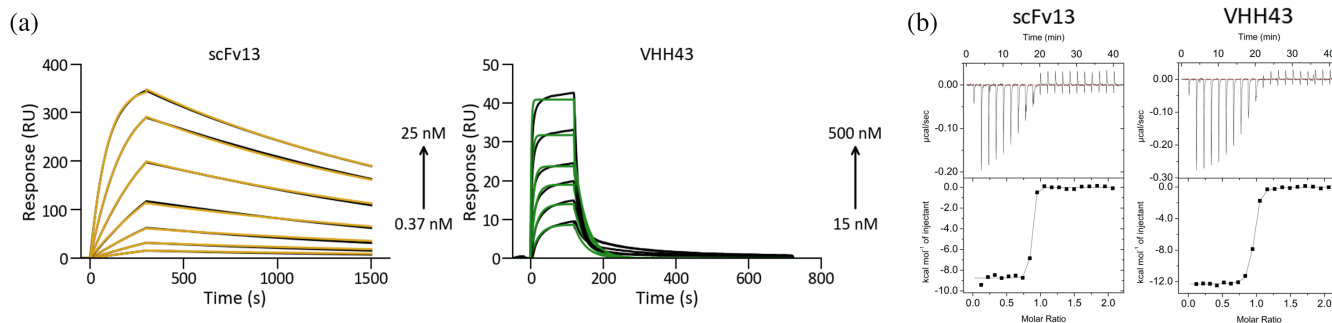
FIGURE 2 Binding of scFv13 and VHH43 to MtsA. (a) SPR data corresponding to the binding of scFv13 and VHH43 to MtsA. Raw sensorgrams of scFv13 and VHH43 and fitted sensorgrams are shown in yellow, green, and black lines, respectively. (b) ITC data corresponding to the binding of scFv13 and VHH43 to MtsA. Representative results are shown.

TABLE 1 Binding parameters of scFv13, VHH43 and GS30 bpAb to MtsA.

Antibody	SPR			ITC				
	k_{on} ($\times 10^5 M^{-1} s^{-1}$)	k_{off} ($\times 10^{-4} s^{-1}$)	K_D (nM)	N (mol:mol)	K_D (nM)	ΔG (kcal mol^{-1})	ΔH (kcal mol^{-1})	$-T\Delta S$ (kcal mol^{-1})
scFv13	5.8 ± 1.1	5.7 ± 0.5	1.0 ± 0.1	0.77 ± 0.05	2.0 ± 1.1	-12 ± 0.5	-8.8 ± 0.2	-2.8 ± 0.7
VHH43	9.0 ± 2.2	233.5 ± 69	27 ± 9.7	0.95 ± 0.03	11 ± 4.4	-11 ± 0.3	-12 ± 0.3	1.2 ± 0.4
scFv13-GS30-VHH43	4.3 ± 0.7	3.2 ± 2.4	0.72 ± 0.46	0.64 ± 0.02	20 ± 28	-11 ± 0.9	-21 ± 0.6	10 ± 1.4

*Note*: Averages and standard deviations of three independent measurements are shown.

and for VHH43 they were $9.0 \times 10^5 M^{-1} s^{-1}$ and $2.3 \times 10^{-2} s^{-1}$. SPR data revealed that the affinity of scFv13 to the antigen was an order of magnitude greater than that of VHH43. We also characterized the interactions using ITC (Figure 2b and Table 1). For scFv13, the measured K_D was 2.0 nM. The enthalpy change (ΔH) and entropic change (ΔS) were determined as -8.8 and -2.8 kcal mol^{-1}, respectively. For VHH43, K_D was 11 nM. ΔH and ΔS were determined as -12 and 1.2 kcal mol^{-1}, respectively. The calculated K_D values were both comparable to the measured values obtained through SPR. These parameters showed the bindings of both scFv13 and VHH43 to MtsA were enthalpy-driven. These results confirmed that the antibodies specifically interacted with MtsA with considerable affinities.

2.3 | Structures of the antibodies in complex with MtsA

To elucidate the epitope of the antibodies, we crystallized the complexes of MtsA with scFv13 or VHH43, respectively. The structure of scFv13 in complex with MtsA was determined by X-ray crystallography at 2.8 Å. The results showed scFv13 bound to the N-terminal lobe on the same side as the entrance of the metal binding pocket (Figure 3a,b and Table 2). The binding of Zn^{2+} ions on MtsA was confirmed through X-ray absorption fine structure measurements. To investigate the impact of scFv13 binding on MtsA structure, the Cα atoms of the N-terminal domain (ASP31-PRO163) were superimposed on scFv13-Zn-bound MtsA and newly solved Zn-bound MtsA structures. The results showed no significant overall structural changes in MtsA due to scFv13 binding, and the positions of the four residues in the metal-binding site were not significantly altered (Figure 3c,d).

Subsequently, we obtained two complex structures involving VHH43 and MtsA: a metal-unbound complex of MtsA and VHH43 referred to as VHH43-metal-unbound MtsA (Figure 4a–c and Table 2) and a Zn^{2+} ion-bound complex of MtsA and VHH43 referred to as VHH43-Zn-bound MtsA (Figure 4d–f and Table 2). VHH43-metal-unbound MtsA was determined at 3.66 Å by X-ray crystallography, while VHH43-Zn-bound MtsA was determined at 1.65 Å. The VHH43 epitope appeared to be positioned obliquely backward from the MtsA metal binding site, suggesting potential binding across the backbone α-helix and the N- and C-terminal domains. Comparison of the VHH43-bound MtsA with the Zn-bound MtsA showed a 4° tilt in the backbone α-helix upon VHH binding (Figure 4g,h). This slight tilt transmitted to the C-terminal domain, which moved outward by about 10°. Among the four metal-binding residues,

Crystal structure of the complex of scFv13 with MtsA. (a) Structure of scFv13 bound to MtsA. scFv13 is colored in blue, and MtsA is in pink. (PDB ID: 8YJ7) (b) Side view of the scFv13-bound MtsA (c) Superposition of scFv13-Zn-bound MtsA with Zn-bound MtsA. Zn-bound MtsA is colored in sky blue, scFv13 is in grayish blue, and scFv13-Zn-bound MtsA is in pink. (d) Superposition of the metal binding site. Zn-bound MtsA is colored in sky blue, scFv13-Zn-bound MtsA is in pink, and Zn is in red. Protein structures were visualized with UCSF Chimera (Pettersen et al., 2004).
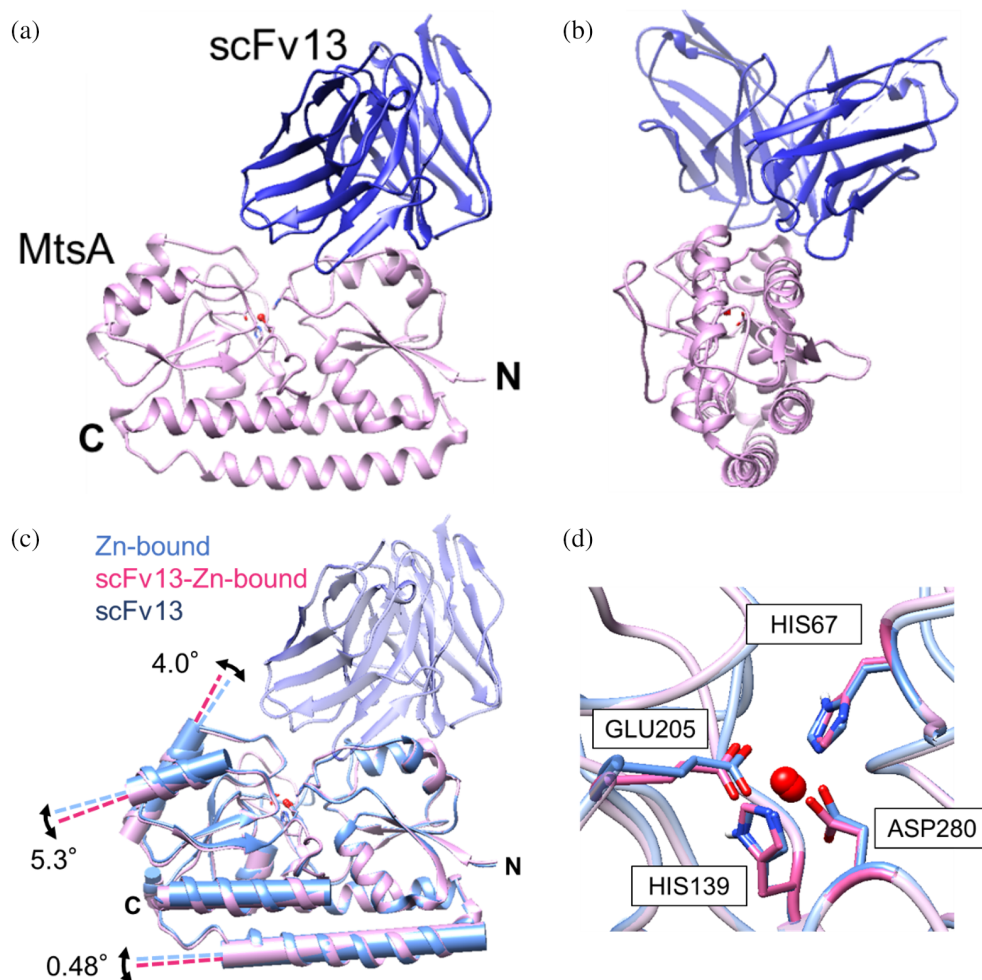
GLU205 and ASP280 from the C-terminal domain shifted 2.2–3.0 and 3.3–3.6 Å away from the metal-binding position, respectively. HIS139 from the N-terminal domain moved 1 Å away from the metal position, and HIS67 flipped towards the solvent side. These findings suggest that VHH43 binding would stabilize an inactive open conformation, leading VHH43-bound MtsA to be less likely to bind to metal. In contrast, the MtsA structure of VHH43-Zn-bound MtsA did not differ from that of Zn-bound MtsA (Figure 4i,j). The positions of the four residues in the metal-binding site were almost identical, indicating that MtsA adopted a closed conformation even in the presence of VHH43. Collectively, these structural analyses suggested that MtsA could adopt both open and closed conformations with bound VHH43, although the binding of VHH43 may influence MtsA conformations and affect metal binding.

2.4 | Design and production of the bpAb

We revealed that the antibodies bound to distinct motifs in MtsA. We designed a bpAb in which scFv13 and VHH43 were connected via an amino acid linker based on crystal structures. When co-crystal structures (PDB: 8YJ7, 8YJ8) were overlaid, the distance between the C-terminus residue of scFv13 and the N-terminus residue of VHH43 was calculated to be 74 Å (Figure 5a). The antibodies were connected via a GS linker, as it is the most commonly used flexible linker and is assumed not to restrict the movement of the antibodies (Chen et al., 2013). Given that the length of the $(G_4S)_6$ linker (referred to as the GS30 linker) was estimated to be 108–114 Å (Chen et al., 2013; Oganesyan et al., 2018; Steinhardt et al., 2018), it was of adequate length to form intramolecular interactions and form the one-to-one complex.

To express the GS30 bpAb as a recombinant protein, the genes encoding each fragment antibody were cloned tandemly into the expression vector pRA2 containing a C-terminal His6 tag (Figure 5b). Expression of two constructs with scFv13 on the N-terminal (scFv13-GS30-VHH43) or C-terminal (VHH43-GS30-scFv13) side was attempted using *E. coli* BL21(DE3) and C43(DE3) strains. Expression in the soluble fraction was confirmed only for scFv-GS30-VHH43 with C43(DE3) (Figure S1).

TABLE 2 Data collection and refinement statistics.

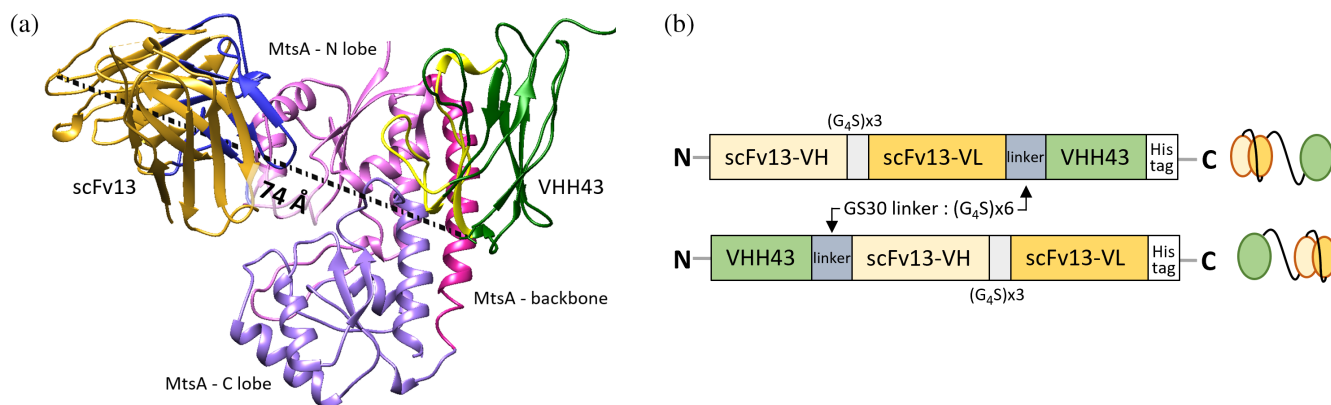|	scFv13 + Zn-bound MtsA	VHH43 + metal-unbound MtsA	VHH43 + Zn-bound MtsA	Zn-bound MtsA
Data collection				
PDB ID	8YJ7	8YJ5	8YJ8	8YJ6
Space group	$P\,2_12_12_1$	$I\,4_1$	$C\,1\,2\,1$	$P\,2_12_12_1$
Unit cell dimensions				
a, b, c (Å)	72.591, 129.272, 245.588	120.45, 120.45, 156.176	292.931, 58.083, 50.76	39.935, 49.828, 147.398
α, β, γ (°)	90, 90, 90	90, 90, 90	90, 91.24, 90	90, 90, 90
Resolution (Å)	48.27–2.8 (2.85–2.8)	47.79–3.66 (4.02–3.66)	35.57–1.65 (1.67–1.65)	38.55–1.37 (1.39–1.37)
Wavelength (Å)	1	1	1	1.282
Total reflections	427,091 (41,468)	94,092 (8950)	3,78,190 (36,717)	6,71,595 (14,751)
Unique reflections	57,771 (2603)	12,349 (3077)	1,01,614 (3190)	54,591 (592)
R_{merge}	20.9 (>1.000)	0.177 (>1.000)	0.070 (>1.000)	0.074 (0.823)
R_{meas}	22.5 (>1.000)	0.190 (>1.000)	0.082 (>1.000)	0.077 (0.896)
$CC_{1/2}$	0.994 (0.637)	0.996 (0.452)	0.997 (0.569)	0.999 (0.727)
$<I/\sigma(I)>$	10.0 (1.6)	7.9 (1.0)	8.4 (1.1)	21.0 (1.6)
Completeness (%)	99.83 (97.45)	99.94 (99.44)	98.88 (90.84)	87.42 (37.00)
Multiplicity	7.38 (7.37)	7.61 (7.24)	3.72 (3.69)	12.3 (6.45)
Wilson B-factor	42.68	148.87	26.54	10.98
Refinement statistics				
Resolution (Å)	48.27–2.8	47.79–3.66	35.57–1.65	38.55–1.37
Reflections used in refinement	57,771 (2603)	12,349 (3077)	1,01,614 (3190)	54,591 (592)
R_{work}	0.2215	0.2631	0.1875	0.1699
R_{free}	0.2761	0.3033	0.2277	0.1937
No. of non-hydrogen atoms	15,165	3141	7048	2685
Macromolecules	15,161	3141	6351	2197
Ligands	4	0	2	1
Solvent	0	0	695	487
Protein residues	1977	405	810	278
Average B-factor (Å^2)	48.11	106.97	35.16	14.84
Macromolecules	48.11	106.97	34.48	12.62
Ligands	75.28		35.71	7.46
Solvent			41.37	24.87
RMSD bond (Å)	0.015	0.023	0.007	0.005
RMSD angle (°)	1.25	2.04	0.87	0.82
Ramachandran plot				
Favored (%)	94.57	94.26	97.26	96.38
Allowed (%)	5.22	4.74	2.37	3.62
Outliers (%)	0.2	1	0.37	0
Clashscore	9.64	7.21	2.78	1.36

FIGURE 4 Crystal structure of the complex of VHH43 with MtsA. (a) Structure of VHH43-metal-unbound MtsA. VHH43 is colored in light blue, and metal-unbound MtsA is in orange. (PDB ID: 8YJ5) (b) Side view of the VHH43-metal-unbound MtsA. (c) Close-up view of the metal binding site. (d) Structure of VHH43-Zn-bound MtsA. VHH43 is colored in light blue, and Zn-bound MtsA is in green. (PDB ID: 8YJ8) (e) Side view of the VHH43-Zn-bound MtsA. (f) Close-up view of the metal binding site. Zn is colored in red. (g) Superposition of VHH43-metal-unbound MtsA with Zn-bound MtsA. Zn-bound MtsA is colored in sky blue, VHH43 is in light blue, VHH43-metal-unbound MtsA is in orange, and Zn is in red. (h) Close-up view of the metal binding site. (i) Superposition of VHH43-Zn-bound MtsA with Zn-bound MtsA. Zn-bound MtsA is colored in sky blue, VHH43-Zn-bound MtsA is in green, and Zn is in red. (j) Close-up view of the metal binding site. Protein structures were visualized with UCSF Chimera (Pettersen et al., 2004).
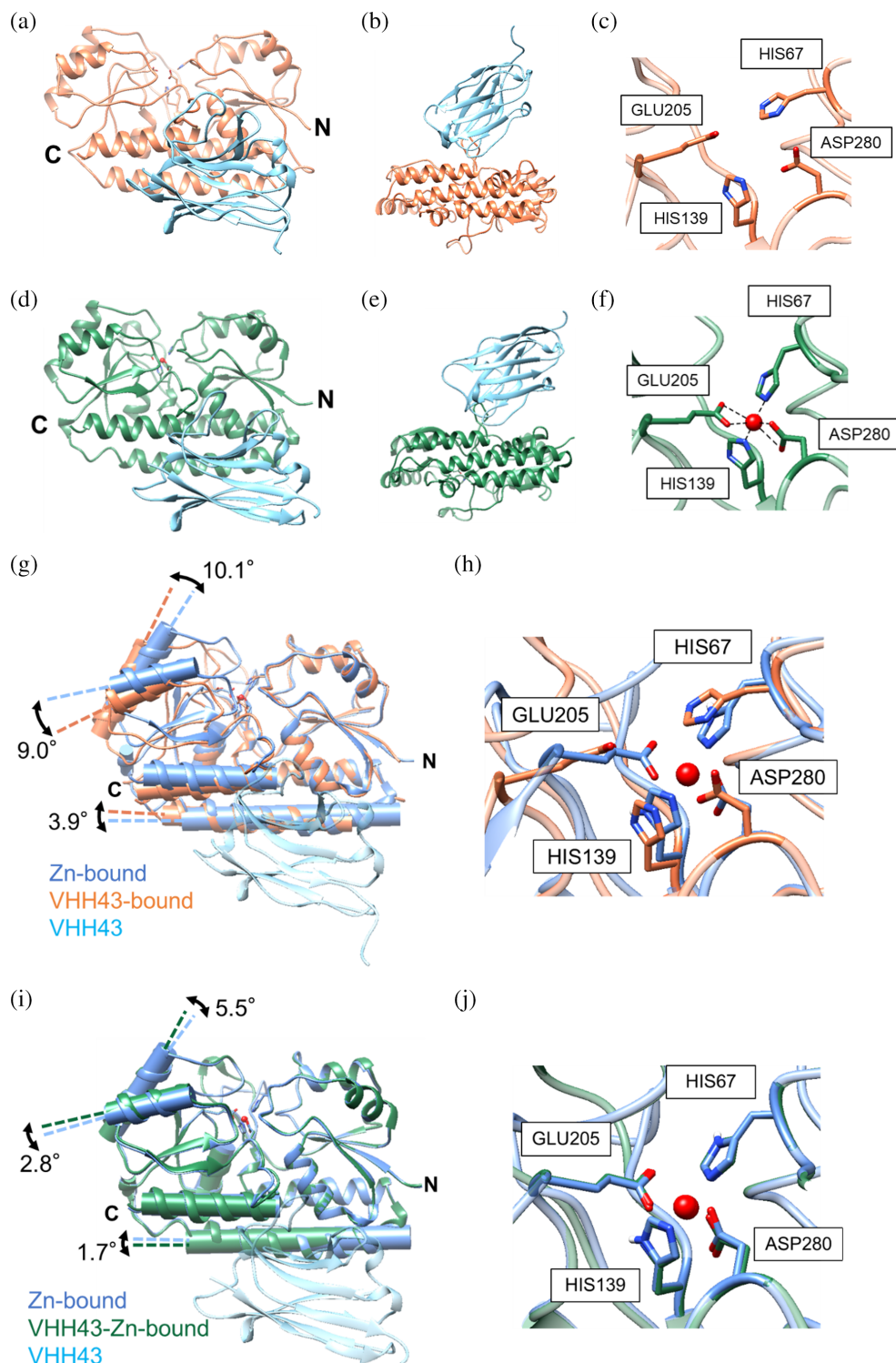

2.5 | Physicochemical characterization of the bpAb

We prepared the GS30 bpAb (scFv13-GS30-VHH43) as a recombinant protein using the *E. coli* expression system and characterized its molecular properties using physicochemical analyses. We then measured the circular dichroism (CD) spectra to assess the secondary structure of the GS30 bpAb. The spectrum for the GS30 bpAb was almost the same as the sum of the scfv13 and VHH43 spectra, suggesting that the folding states of individual antibodies were the same as those of the original antibodies (Figure 6a). The subtle differences in the signals may be due to the linker. We also analyzed the thermal stability of the bpAb using differential scanning calorimetry (DSC) and found that the peak tail corresponded to

FIGURE 5 Design of the bpAb based on crystal structure. (a) Superposition of scFv13-bound MtsA with VHH43-metal-unbound MtsA. The dotted lines show the distance between Cα atoms of the C-terminus residue of scFv13 and the N-terminus residue of VHH43. scFv13 is shown in gold, the CDR of scFv13 is in blue, VHH43 is in green, the CDR of VHH43 is in yellow, the N-lobe of MtsA is in pink, the C-lobe of MtsA is in purple, and the backbone of MtsA is in magenta. Protein structures were visualized with UCSF Chimera (Pettersen et al., 2004). (b) Constructs of scFv-VHH bpAb. scFv13 is linked to VHH43 by the amino acid linker composed of four glycines and one serine repeated six times [(G_4S)x6] at both the N- or C-terminus.
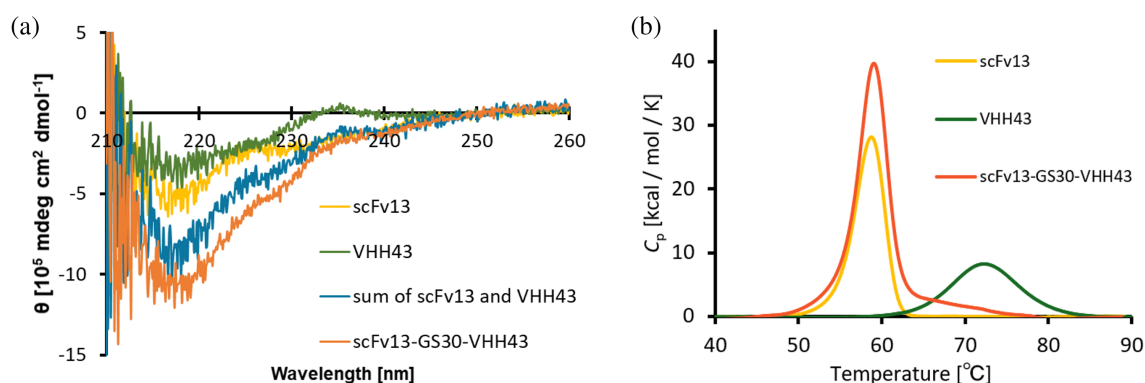
FIGURE 6 Physicochemical properties of the GS30 bpAb. (a) CD spectra of the antibodies. scFv13 is shown in yellow, VHH43 is in green, the sum of scFv13 and VHH43 is in blue, and the GS30 bpAb is in orange. (b) Thermal stability of the antibodies determined by DSC. scFv13 is in yellow, VHH43 is in green; and the GS30 bpAb is in orange. Representative results are shown.

the melting temperature (T_m) of 59.0°C (Figure 6b and Table 3). Importantly, ΔH of the GS30 bpAb was almost the same as the sum of those of scFv13 and VHH43. The DSC analysis of single scFv13 and VHH43 showed that each single peak had T_m values of 58.6 and 72.4°C, respectively.

2.6 | Binding characteristics of the bpAb against MtsA

We used SPR and ITC to quantitatively evaluate the binding of the bpAb to MtsA. SPR measurements showed almost same K_D, k_{on}, and k_{off} values compared with scFv13 (Figure 7a and Table 1). Importantly, ITC analysis showed that ΔH upon binding of the bpAb was the same

TABLE 3 Melting temperature (T_m) and ΔH values of the GS30 bpAb.

	T_m (°C)	ΔH (kcal mol^{-1})
scFv13	58.6	131
VHH43	72.4	86
scFv13-GS30-VHH43	59.0	221

as the sum of ΔH upon scFv13 and VHH43 binding (Figure 7b and Table 1), suggesting that scFv13 and VHH43 simultaneously bound to MtsA. Additionally, the binding of the GS30 bpAb exhibited a larger positive ΔS than that of either of the fragment antibodies. This unfavorable entropic change might be originated from restriction of the linker fluctuation upon binding.
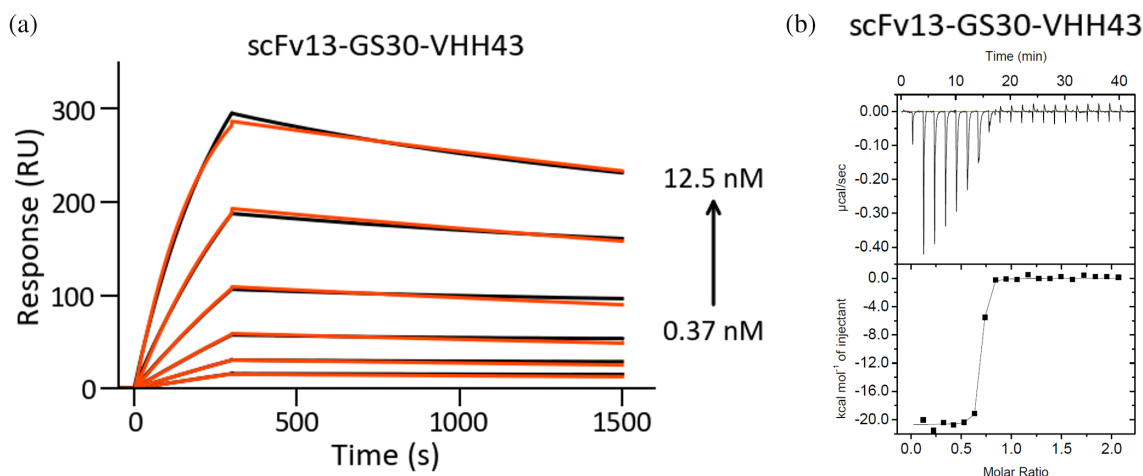
FIGURE 7 Binding of the GS30 bpAb to MtsA. (a) SPR data corresponding to the binding of the GS30bpAb to MtsA. Raw sensorgrams and fitted curves are shown in orange and black lines, respectively. (b) ITC data corresponding to the binding of the GS30 bpAb to MtsA. Representative results are shown.

2.7 | Complex formation of the bpAb with the GS30 linker

We analyzed the complex state of the bpAb and MtsA using size-exclusion chromatography coupled with multi-angle light scattering (SEC-MALS) analysis to measure absolute molecular weight of the purified bpAb:MtsA complex. Contrary to expectation, bpAb and MtsA mainly formed a 2:2 complex with 146 kDa molecular weight (MW), but a smaller fraction of a 3:3 complex with 220 kDa MW was also detected (Figure 8a). We collected the complexes in the fraction mainly consisting of 3:3 complexes and observed them using a negative stain transmission electron microscope (nsTEM). A representative micrograph is shown as Figure 8b. Although various sizes and shapes of complexes were observed, likely due to the equilibrium of the complexes or the effect of fixation, some of them formed ring-shaped complexes. Intriguingly, the size of a representative triangular complex fit the model structure of the 3:3 complex (Figure 8c, d). We then conducted two-dimensional (2D) classification to ensure the presence of ring-shaped complexes (Figure 8e). The result indicated the presence of numerous ring-shaped complexes of varying sizes, but triangular complexes emerged as the major structure.
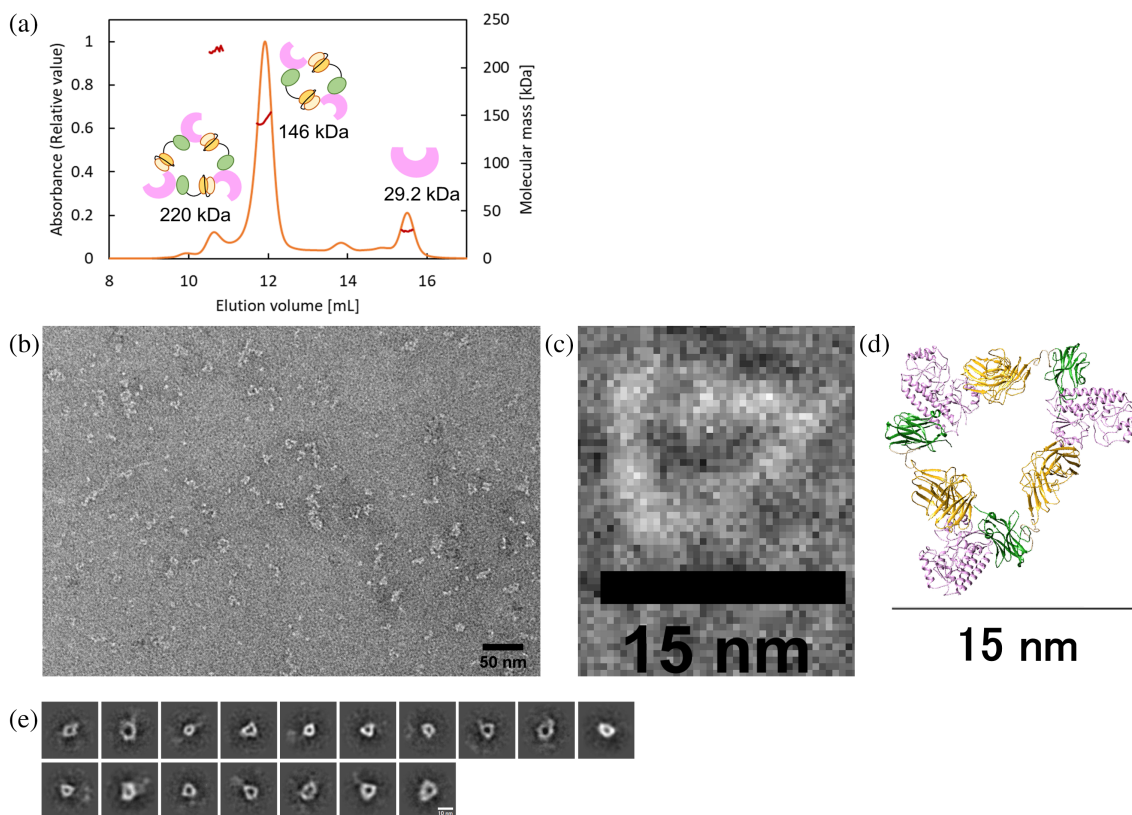
2.8 | Comparison of complex formation of the bpAb with various linkers

As observed above, the GS30 bpAb formed intermolecular complexes. We next examined the relationship between the linker length and the complex association state. GS linkers of 5 and 20 residues were adopted as short linkers. We attempted to produce GS linkers with

60 residues, but genetic engineering did not work due to the high GC content. Therefore, we selected a PAS linker consisting of proline, alanine, and serine, which is uncharged with a theoretically random coil structure. It has high solubility and can be lengthened up to several hundred residues (Lerchner et al., 2016; Schlapschy et al., 2013) to create a bpAb with a 60 amino acid length linker. The linker sequences are shown in Table S1.

We prepared each construct as a recombinant protein and mixed it with equimolar amounts of MtsA to assess the assembly states of bpAb complexes using SEC-MALS (Figure 9). Based on the calculated molecular weights, GS5 predominantly formed 3:3 complexes with potential formations of 4:4 and 5:5 complexes. While the primary complex for GS20 was calculated as 190 kDa, suggesting the ability to form a bpAb:MtsA = 3:2 complex, 2:2 and 3:3 complexes also formed as minor fractions. Collectively, it became apparent that larger multimeric complexes formed as the GS linker length decreased. In contrast, the longer linker PAS60 mainly formed a 1:1 intermolecular complex of 76 kDa. Although 2:2 intramolecular complexes were also present, we successfully produced an intramolecular complex by lengthening the linker.

To assess the presence of an equilibrium between the complexes, each complex fraction was collected and reinjected into the analytical SEC with different time scales after separation. Mixed GS30 bpAb and MtsA in a molar ratio of 1:1.2 was injected into the SEC, and the 3:3 and 2:2 complexes were collected separately. Within several hours, the complexes were reinjected into the SEC with adjusted concentration. The results of the 3:3 complexes revealed that not only the presence of the 3:3 complex peak but also the emergence of a peak of 2:2 complexes, confirming the existence of an equilibrium between

FIGURE 8 Complex formation of the GS30 bpAb with MtsA. (a) SEC-MALS of the GS30 bpAb and MtsA complex. Orange lines represent relative value of absorbance at 280 nm. Red lines represent molecular weight. (b) Representative nsTEM micrograph of the GS30bpAb:MtsA complex. (c) Close-up view of a representative GS30bpAb:MtsA ring-shaped complex. (d) Model structure of the 3:3 complex. The scale bar represents 15 nm. Protein structures were visualized with UCSF Chimera (Pettersen et al., 2004). (e) 17 representative 2D nsTEM class averages of the ring-shaped GS30 bpAb:MtsA complex. The scale bar represents 10 nm.
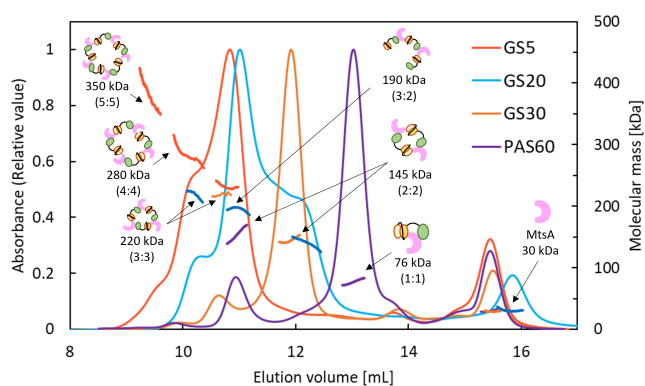

FIGURE 9 Complex formation of the bpAb linked by various linkers. SEC-MALS of bpAbs with various linkers and the MtsA complex. Relative value of absorbance at 280 nm and molar mass are represented by thin and bold lines, respectively. GS5 is shown in dark orange, GS20 is in blue, GS30 is in orange, and PAS60 is in purple.

complexes (Figure 10a). Additionally, the 3:3 complex emerged from the 2:2 complexes (Figure 10b). We repeated the experiment 7 days later, and no significant

change in the state of complex formation was observed. As for the PAS60 bpAb complexes, we collected the 2:2 and 1:1 complexes separately and subjected them to SEC with adjusted concentration. From the 2:2 complexes, a distinct 1:1 complex peak emerged alongside the 2:2 complex peak within several hours (Figure 10c). Following a 7-day incubation at 4°C, the amount of 1:1 complex increased, leading to a decrease in the amount of 2:2 complexes. In contrast, when the 1:1 complex was injected, the 2:2 complex peak did not appear, even after 7 days (Figure 10d). In summary, transition of the complex state was observed for both GS30 bpAb and PAS60, although the stable complex differed between the two constructs.

2.9 | Blocking the metal binding of MtsA with the GS30 linker bpAb

Finally, we used ITC to assess whether the bpAb affected the metal binding of MtsA (Figure 11 and Table 4). Exothermic reactions were observed for the titration of
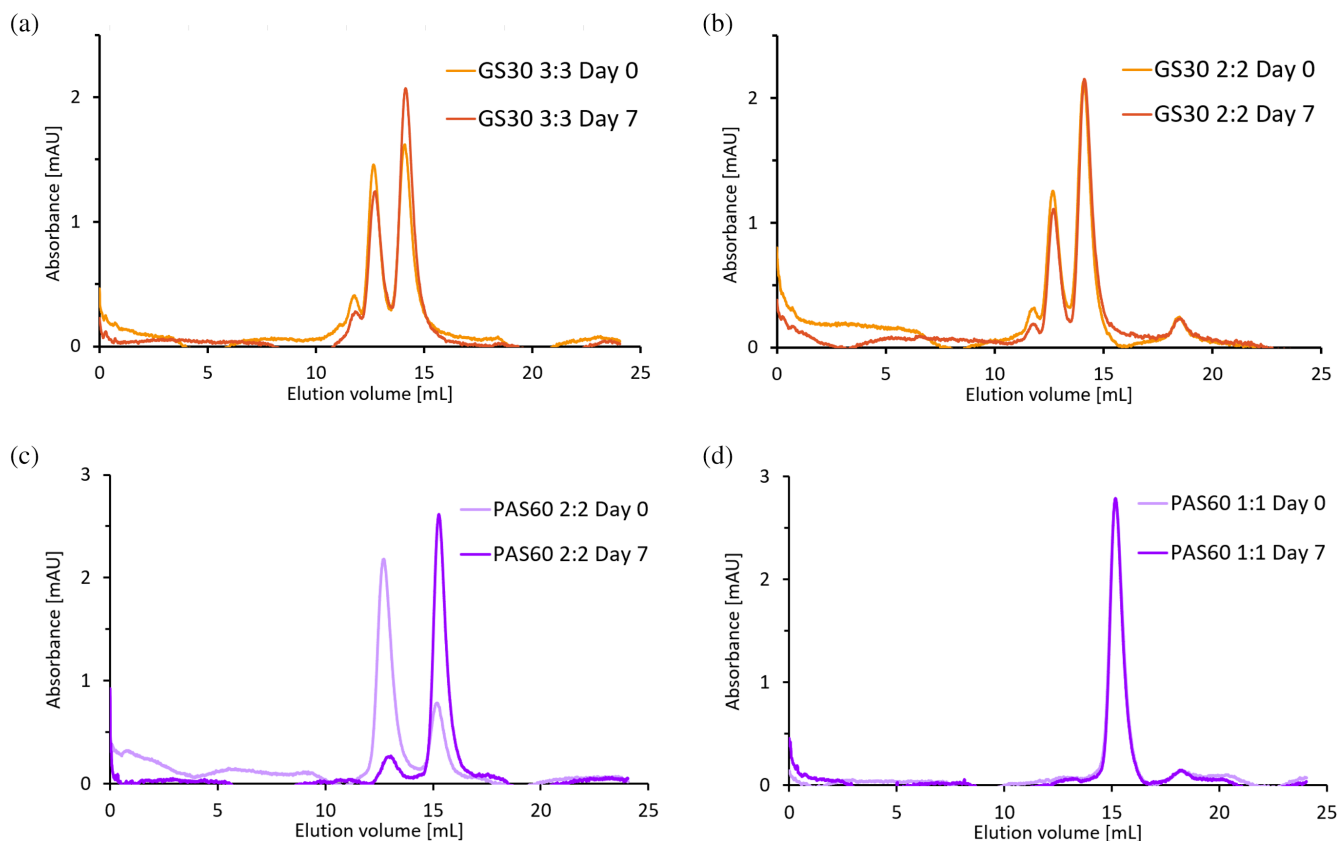
FIGURE 10 Equilibrium between bpAb and MtsA complexes. Analytical SEC of fractioned the bpAb and MtsA complex. Ultraviolet absorbance at 280 nm is represented. (a) Reinjection of the 3:3 complex of GS30 bpAb and MtsA (orange: day 0, brown: day 7). (b) Reinjection of the 2:2 complex of GS30 bpAb and MtsA (orange: day 0, brown: day 7). (c) Reinjection of the 2:2 complex of PAS60 bpAb and MtsA (light purple: day 0, purple: day 7). (d) Reinjection of the 1:1 complex of PAS60 bpAb and MtsA (light purple: day 0, purple: day 7).

manganese ion (Mn^{2+}) against MtsA, with stoichiometry of 0.72 ± 0.09 (Figure 11a). In the presence of two equivalent molecules of scFv13, the enthalpic change upon Mn^{2+} binding decreased by about 2 kcal mol^{-1}, and the stoichiometry decreased from 0.80 to 0.66 (Figure 11b). This result suggested that scFv13 antibodies affected the Mn^{2+} binding properties of MtsA but that this effect was insufficient to inhibit metal binding. On the other hand, in the presence of two equivalent molecules of VHH43, the enthalpic change upon Mn^{2+} binding decreased by 0.64 kcal mol^{-1}, and no change in stoichiometry was observed (Figure 11c). When scFv13 and VHH43 were simultaneously added to MtsA, the stoichiometry and the binding enthalpy decreased to about the same extent as that observed for scFv13 alone (Figure 11d). Next, we examined the metal binding inhibition of MtsA by GS30 bpAb and PAS60 bpAb, hypothesizing that two antibodies connected via an amino acid linker would further affect the Mn^{2+} binding to MtsA. However, none of them caused complete inhibition, although the parameters changed to some extent (Figure 11e,f). Collectively, these results indicated that only scFv13 could influence the equilibrium of

the MtsA-Mn^{2+} interaction and that simultaneous binding of bpAb to distinct epitopes on MtsA did not impact the metal binding activity.

3 | DISCUSSION

In this study, we successfully developed and characterized a novel format scFv-VHH bpAb against MtsA. While various formats of bpAbs for fragment antibodies have been developed, herein we report a novel construct. Combining two fragment antibodies with distinct epitopes and binding affinities via a GS30 linker did not result in formation of the intramolecular 1:1 complex. The thermodynamic parameters of ITC indicated that both scFv13 and VHH43 simultaneously bound to MtsA. However, the GS linker can adopt an unstructured, random coil conformation (Evers et al., 2006), so the average end-to-end distance of the linker would be shorter than calculated. The linker length may not be enough to form an intramolecular binding complex. Indeed, extending the linker to 60 residues (i.e., the PAS60 linker), resulted in
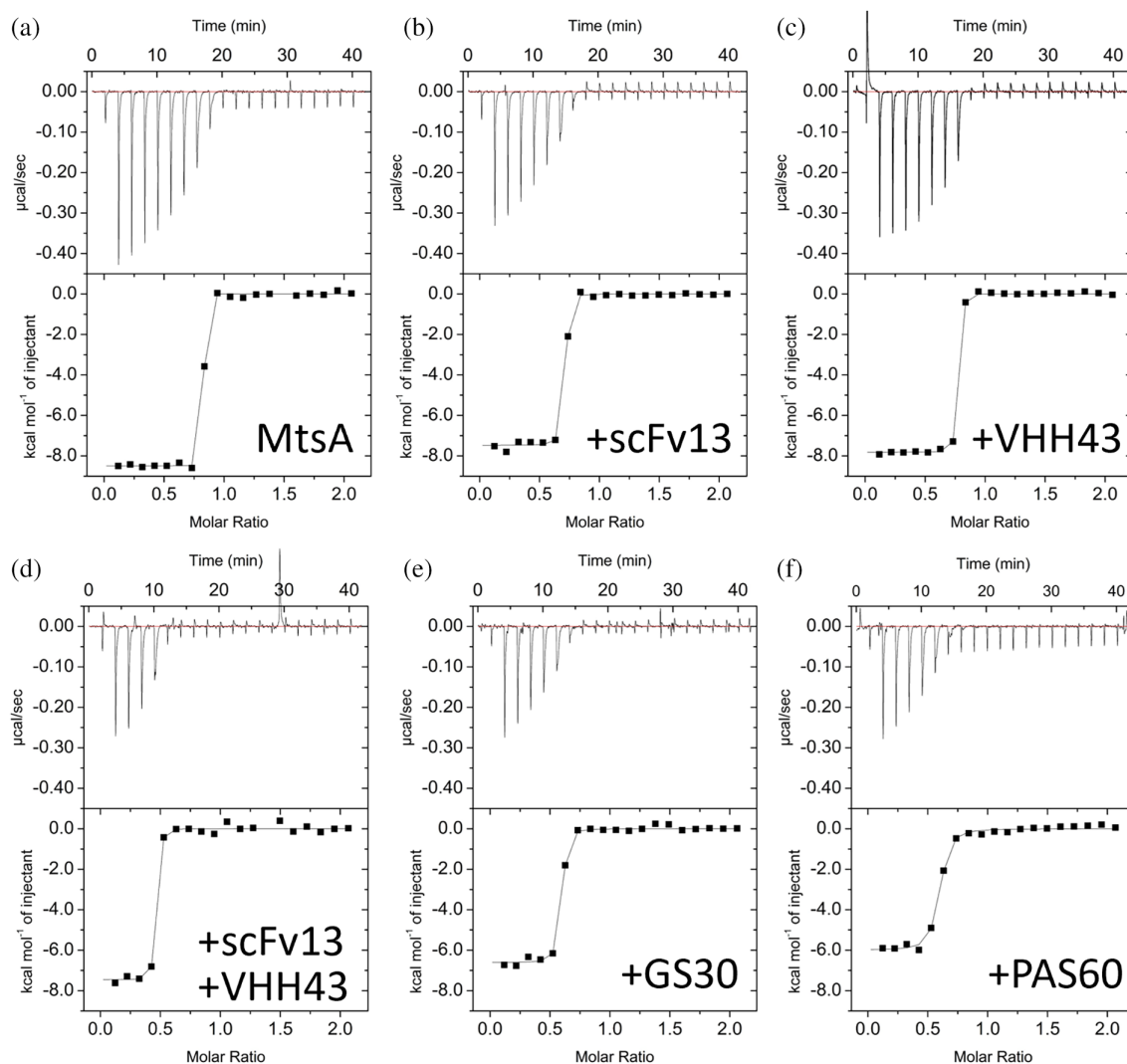
FIGURE 11 Metal binding inhibition of the bpAb. Titration curve of the ITC analysis of the interaction between Mn^{2+} and MtsA in the presence of 2M equivalent antibodies: (a) buffer, (b) scFv13, (c) VHH43, (d) scFv13 and VHH43, (e) GS30 bpAb (scFv13-GS30-VHH43), and (f) PAS60 bpAb (scFv13-PAS60-VHH43). Representative results are shown.

TABLE 4 Binding parameters of manganese ion to MtsA with antibodies.

	N	ΔH (kcal mol^{-1})
MtsA	0.796	−8.42
+2 mol equiv. scFv13	0.659	−7.48
MtsA	0.776	−8.49
+2 mol equiv. VHH43	0.731	−7.85
MtsA	0.749	−10.3
+2 mol equiv. scFv13, VHH43	0.423	−7.46
MtsA	0.667	−8.74
+2 mol equiv. scFv13-GS30-VHH43	0.546	−6.61
MtsA	0.697	−8.21
+2 mol equiv. scFv13-PAS60-VHH43	0.554	−6.00

bpAb and MtsA forming the 1:1 complex via intramolecular crosslinking. In contrast, shortening the linker resulted in the formation of larger multimeric complexes. These results indicate that linker length significantly influenced the complex formation states. We assume that the determining factor for the complex formation state is spatial accessibility constraint. Initially, either of the fragment antibodies binds to MtsA, followed by the other antibody binding to MtsA. In this step, it would be difficult for the other antibody connected by a short linker to the first antibody to bind to the already antibody-bound MtsA due to spatial limitations. Thus, bpAb with shorter linkers tended to form larger complexes. Given that PAS linkers are thought to be less flexible than GS linkers (Gräwe et al., 2020; Schlapschy et al., 2013), linkers with varied rigidity, surface charge, and hydrophilicity may result in different complex formation behavior.

The results of the SEC analysis indicated that there is an equilibrium state in the ratio of complexes depending on linker length. Even if complexes with certain association state are isolated, the association state changes to meet the equilibrium condition. The speeds of reaching equilibrium state are likely different depending on the length of linkers. Nevertheless, we observed a variety of complexes, including a 3:2 complex, for GS20 in the SEC-MALS analysis. The simultaneous formation of different sized complexes may be due to the unbalanced affinity between scFv and VHH, resulting in complexes in kinetic transition states. Considering that the analytical SEC experiments were conducted with diluted samples through the first SEC, the concentration of the samples may also have affected the association states. Considerations on transition states of complexes may be important for further development of bpAbs depending on mechanism of their actions.

A critical feature of the bpAb developed in this study is its asymmetric structure, which connects different formats of fragment antibodies. Indeed, it showed distinct characteristics compared with previously developed bpAbs. The DSC analysis of single scFv13 and VHH43 showed that each single peak had T_m values of 58.6 and 72.4°C, respectively. Given that bpAb had the almost identical melting temperature with scFv13 and denatured in a single peak with larger enthalpic change, VHH43 portion would denature simultaneously with scFv13. The CD analysis revealed that the folding states of individual antibodies were likely to be the same as those of the original antibodies, thus scFv13 and the flexible linker would destabilize the VHH43 kinetically. These results align with a previous report about linked VHHs that demonstrated that the unfolding of VHHs with higher T_m values coincided with the simultaneous unfolding of the other VHHs[39]. As for binding to the antigen, the thermodynamic parameters of the interaction with MtsA were close to the combination of scFv13 and VHH43, indicating simultaneous binding of scFv13 and VHH43. Nevertheless, the improvement in kinetic parameters was limited compared to previous studies showing that linking VHHs or VHs, which bind to different epitopes with a 20-amino-acid glycine-serine linker, resulted in a significantly slower k_{off} (Bracken et al., 2021; Henry et al., 2021; Wagner et al., 2021; Walter et al., 2022). This result may be due to the large affinity gap between the two antibodies. Also, as researchers previously reported that the order of the fragment antibodies in the bpAb constructs significantly affected the affinity (Glaven et al., 2012), the relative position of paratopes in each fragment antibody would be critical to their avidity effect. Alternatively, because MtsA was immobilized on a sensor chip in our SPR experiments, both epitopes for scFv13 and VHH43 may not have been exposed. Connecting

antibodies with similar affinities and/or different epitopes might improve the avidity effect.

nsTEM observations successfully captured the ring-shaped 3:3 complex, supporting the results of the SEC-MALS analysis. Because there is an equilibrium between complexes, we expected the 2:2 complex to be present on the grids. However, we were unable to clearly distinguish the 2:2 complex from various sized particles. In contrast, we did observe larger complexes exceeding 3:3 and string-like structures. The sample preparation steps for nsTEM, such as fixation on the grid and drying, may have affected complex formation (Ohi et al., 2004).

We obtained co-crystal structures for each antibody with MtsA, and we were particularly successful in obtaining the co-crystal structure of VHH43 with metal-unbound MtsA at 3.66 Å. The low resolution may suggest the high structural flexibility of metal unbound MtsA. Although the structure implied that the binding of VHH43 to MtsA could potentially influence metal binding of MtsA, no significant changes were observed in the ITC experiments. As the affinity of VHH43 is lower than that of metals and it does not directly bind to the metal binding pocket, the actual impact on metal binding might be limited. Moreover, the crystallization might represent a snapshot of metal-unbound MtsA, which would not be in equilibrium state. On the other hand, scFv13 appeared to affect the metal binding of MtsA. The structural analysis suggested that scFv13 bound to the epitope near the metal binding pocket and suppressed N-lobe movement upon metal binding. Therefore, we hypothesized that the bpAb binding at two sites astride the N- and C- lobes simultaneously could further constrain the conformation of MtsA and potentially inhibit metal binding. However, the decrease in stoichiometry was comparable to that of scFv13 alone, and no inhibitory effect was observed. For tiny ligands like metals, a direct inhibition approach might be more effective.

In conclusion, this is the first report of the development of a scFv-VHH format bpAb, and we evaluated its properties using physicochemical approaches. These results provide important insight into the design strategy of fragment-based bpAbs against new targets. We believe that this work will promote the creation of novel bpAbs with desired functions.

4 | METHODS

4.1 | Expression and purification of recombinant MtsA

The gene encoding MtsA (31–310) was amplified, and the PCR products were inserted into a pColdI vector with an N-terminal His6 SUMO tag. *E. coli* strain BL21(DE3)

transformed with the vector was grown at 37°C in lysogeny broth (LB) medium supplemented with 50 μg/mL ampicillin. When optical density (OD_{600}) reached 0.5, protein expression was induced by adding isopropyl β-D-1-galactopyranoside (IPTG) at a final concentration of 0.5 mM for 24 h at 20°C. Cells were harvested by centrifugation at 7000 × g for 10 min, and the pellet obtained was resuspended with 20 mM Tris–HCl (pH 8.0), 500 mM NaCl, 5 mM imidazole. Cells were subsequently sonicated for 20 min with an ultrasonic cell-disruptor instrument (TOMY, Tokyo, Japan). The supernatant containing the soluble intracellular components was obtained by ultracentrifugation at 40,000 × g for 30 min. The soluble fraction was applied to the column filled with a Ni-NTA agarose (QIAGEN, Hilden, Germany) equilibrated with 20 mM Tris–HCl (pH 8.0), 500 mM NaCl, 5 mM imidazole. The column was washed sequentially with 20 mM Tris–HCl (pH 8.0), 500 mM NaCl, 5 mM imidazole, and His6 SUMO tagged MtsA was eluted with 100 mM imidazole in 20 mM Tris–HCl (pH 8.0), 500 mM NaCl. The eluted protein was mixed with His6-tagged SUMO protease 1 (Ulp1) and dialyzed at 4°C overnight in 20 mM Tris–HCl (pH 8.0), 500 mM NaCl, 5 mM imidazole. The solution was loaded onto a Ni-NTA agarose column to remove uncut MtsA, the cut tags, and the added protease. To remove any metal ions, the flow through was dialyzed at 4°C overnight in 5 mM EDTA with 50 mM HEPES-NaOH (pH 7.5), 200 mM NaCl, 300 μM $NaHCO_3$ and then subjected to size exclusion chromatography (SEC) with a Hiload 26/60 Superdex 75 pg column (Cytiva, Marlborough, MA, USA) equilibrated with 50 mM HEPES-NaOH (pH 7.5), 200 mM NaCl, 300 μM $NaHCO_3$. The monomer peak fraction was collected. For ITC experiments, MtsA was further purified to remove metal-bound MtsA. The flow through of His-SUMO tag cut MtsA was dialyzed at 4°C overnight in 50 mM HEPES-NaOH (pH 7.5), 20 mM NaCl, 5 mM EDTA, and anion-exchange chromatography was performed using a Resource™ Q 1 mL column (Cytiva). The column was washed with 50 mM HEPES-NaOH (pH 7.5), 20 mM NaCl before injection of the protein. After injection of the protein, the column was washed with 50 mM HEPES-NaOH (pH 7.5), 20 mM NaCl. Then, 50 mM HEPES-NaOH (pH 7.5), 200 mM NaCl, 300 μM $NaHCO_3$ was added to elute the protein. Eluted fractions were collected for ITC analysis.

4.2 | Generation of scFv13

A rabbit was immunized with recombinant MtsA to generate single-chain variable fragments (scFvs). MtsA was injected four times every 2 weeks. After verifying the elevation of antibody titer in rabbit serum against MtsA,

total RNA was isolated from the rabbit spleen using Sepasol®-RNA I Super G (Nacalai Tesque, Kyoto, Japan). The cDNA was prepared by reverse transcription using the PrimeScript™ 1st strand cDNA Synthesis Kit (TaKaRa, Shiga, Japan), and the variable domain sequences of the heavy and light chains were amplified by PCR using Q5 High-Fidelity DNA Polymerase (New England Biolabs, Ipswich, MA, USA). PCR products were isolated by 2.0% agarose gel electrophoresis and purified using Nucleo Spin Gel and PCR Clean-up (Macherey-Nagel, Dürin, Germany). Heavy and light strand DNAs were inserted into the pADL23c vector using NEBuilder HiFi DNA Assembly (New England Biolabs), and the plasmids were purified with Agencourt AMPure XP (Beckman Coulter, Brea, CA, USA). TG1 electrocompetent cells were transformed with the scFv library by electroporation. The scFvs were selected by panning using MtsA-immobilized immunotubes and evaluated by ELISA assay. The 13th clone, which showed specific binding to MtsA, was named scFv13.

4.3 | Generation of VHH43

An alpaca was immunized with recombinant MtsA to generate heavy chain only antibodies. Seven weeks after the injection, lymphocytes were collected from the blood, and the total RNA was isolated with TRIZOL reagent (Thermo Fisher Scientific, Waltham, MA, USA). The cDNA was prepared by reverse transcription using Super ScriptIII Reverse Transcriptase (Thermo Fisher Scientific), and the variable domain of the heavy chain only antibody (VHH) sequences were amplified by PCR using Q5 High-Fidelity DNA Polymerase. The PCR products were isolated by 0.8% agarose gel electrophoresis and purified with Nucleo Spin Gel and PCR Clean-up. The VHH DNA was inserted into the pLUCK2001Q4 vector using NEBuilder HiFi DNA Assembly, and the plasmids were purified with Agencourt AMPure XP. TG1 electrocompetent cells were transformed with the VHH library by electroporation. The VHHs were selected by panning using MtsA-immobilized immunotubes and evaluated by ELISA assay. The 43rd clone, which showed specific binding to MtsA, was named VHH43.

4.4 | Expression and purification of scFv13/VHH43

The DNA of fragment antibodies were inserted into a pRA2 vector, respectively. A His6 tag was added at the C-terminus of the protein. To promote the expression of the periplasmic region, the pelB leader sequence was placed at the N-terminus. *E. coli* strain BL21(DE3) transformed

with the vector was grown at 28°C in LB medium supplemented with 50 μg/mL ampicillin. When OD_{600} reached 0.8, protein expression was induced by adding 0.5 mM IPTG for 20 h at 20°C. Cells were harvested by centrifugation at $7000 \times g$ for 10 min, and the pellet was resuspended with 20 mM Tris–HCl (pH 8.0), 500 mM NaCl, 5 mM imidazole. Cells were subsequently sonicated for 20 min with an ultrasonic cell-disruptor instrument. The supernatant containing the soluble intracellular components was obtained by ultracentrifugation at $40,000 \times g$ for 30 min. The soluble fraction was applied to a Ni-NTA agarose column equilibrated with 20 mM Tris–HCl (pH 8.0), 500 mM NaCl, 5 mM imidazole. The column was washed sequentially in 20 mM Tris–HCl (pH 8.0), 500 mM NaCl, 50 mM imidazole, and each His6 tagged antibody was eluted with 20 mM Tris–HCl (pH 8.0), 500 mM NaCl, 200 mM imidazole. The eluted protein was subjected to SEC with a Hiload 26/60 Superdex 75 pg column equilibrated with 50 mM HEPES-NaOH (pH 7.5), 200 mM NaCl, 300 μM $NaHCO_3$. The monomer peak fraction was collected.

4.5 | Expression and purification of bpAbs

scFv13 and VHH43 were genetically linked using different linkers (Table S1) and cloned into pRA2 vector with a C-terminal His6 tag and N-terminal pelB leader sequence. *E. coli* strain C43 (DE3) transformed with the vector was grown at 28°C in LB medium supplemented with 50 μg/mL ampicillin. When OD_{600} reached 0.8, protein expression was induced by adding 0.5 mM IPTG for 20 h at 20°C. Cells were harvested by centrifugation at $7000 \times g$ for 10 min, and the pellet obtained was resuspended in 20 mM Tris–HCl (pH 8.0), 500 mM NaCl, 5 mM imidazole. Cells were subsequently sonicated for 20 min with an ultrasonic cell-disruptor instrument. The supernatant containing the soluble intracellular components was obtained by ultracentrifugation at $40,000 \times g$ for 30 min. The supernatant of the cell culture, the soluble fraction, and the insoluble fraction were analyzed by SDS-PAGE and western blotting to check the expression of the bpAb in each fraction. The bpAb was purified from soluble fraction following the same method as that used for fragment antibodies.

4.6 | Crystallization of metal-bound MtsA

Purified MtsA was dialyzed in 10 mM Tris–HCl (pH 8.0) and 30 mM NaCl. The sample was concentrated to 10 mg/mL prior to crystallization experiments. The optimal conditions for crystallization were determined using an Oryx8 instrument (Douglas Instruments, Berkshire, UK) and Index (Hampton Research, Alisa Viejo, CA, USA). The crystal used for data collection was obtained in a crystallization solution containing 0.2M $MgCl_2$, 0.1M Tris (pH 8.5), 25% w/v PEG3350.

4.7 | Crystallization of antibody-bound MtsA

Purified antibody (scFv13 or VHH43) was mixed with purified MtsA and subjected to SEC to purify the complex in 50 mM HEPES-NaOH (pH 7.5), 200 mM NaCl, 300 μM $NaHCO_3$. The fractions containing complex were separately dialyzed in 10 mM Tris–HCl (pH 8.0) and 30 mM NaCl. The fractions were pooled together and concentrated to 10 mg/mL prior to the crystallization experiments (hanging drop). The optimal conditions for crystallization were determined using an Oryx8 instrument using Index and PEG/Ion screen kits (Hampton Research). For the scFv13-Zn-bound MtsA complex, the crystallization solution consisted of 0.05M zinc acetate dihydrate and 20% w/v PEG 3350. For the VHH43-metal-unbound MtsA complex, the solution contained 1.8M ammonium citrate tribasic (pH 7.0). For the VHH43-Zn-bound MtsA, the solution contained 0.2M ammonium sulfate and 20% w/v PEG 3350. Suitable crystals were harvested, briefly incubated in mother liquor supplemented with 20% glycerol, and transferred to liquid nitrogen for storage.

4.8 | Data collection and refinement

Data collection was performed on BL26B2 (Ueno et al., 2006) at SPring-8. The collected diffraction images were processed with XDS (Kabsch, 2010). For the MtsA-Zn ion complex structure, X-ray Absorption Fine Structure (XAFS) was performed to determine the wavelength used in the single wavelength anomalous dispersion (SAD) method. Based on the XAFS result, the dataset was collected at a wavelength of 1.282 Å. Experimental phases for the MtsA-Zn complex structure were determined using the 1.37 Å resolution SAD dataset. Determining the heavy atom sub-structure using SAD and subsequent initial structure determination was determined by Crank2 software (Potterton et al., 2018), followed by model building using phenix.autobuild (Adams et al., 2010) and structure refinement using phenix.refine and coot (Emsley et al., 2010). The structures of scFv13-Zn-bound MtsA, VHH43-metal-unbound MtsA, and VHH43-Zn-bound MtsA were determined using PDB ID 3HH8 (MtsA), 6PIL (scFv), and 7KN7 (VHH) with

phenix.phaser. The initial structures were model built with phenix.autobuild and refinement was performed with phenix.rosetta_refine, phenix.refine and coot.

4.9 | SPR analysis of antibody binding

Interaction analysis between MtsA and antibodies was conducted using a Biacore T200 instrument (Cytiva). The antibodies were immobilized on a CM5 chip (Cytiva) by amine coupling (Fischer, 2010) with acetate at pH 4.5 and with an immobilization level aim of 500 RU for scFv13 and GS30 bpAb and 900 RU for VHH43. The activated surface of the sensor was blocked with 1M ethanolamine. The interactions between MtsA and antibodies were measured by injecting increasing concentrations of antibodies into the sensor chip at a flow rate of 30 μL/min. Measurement of the interaction was carried out in 50 mM HEPES-NaOH (pH 7.5), 200 mM NaCl, 300 μM NaHCO$_3$, 0.005% (v/v) Tween20 at 25°C. Antibody binding was measured in a multicycle manner with concentrations of scFv13 ranging from 0.37 to 25 nM, VHH43 ranging from 15 to 500 nM, and GS30bpAb ranging from 0.37 to 12.5 nM, and the regeneration steps were performed with 10 mM glycine–HCl at pH 2.0 (Cytiva). The SPR data were analyzed using BIAevaluation software (Cytiva).

4.10 | ITC analysis of antibody binding

The ITC experiments were performed using an iTC200 microcalorimeter (Malvern Panalytical, Malvern, UK). The antibodies were dialyzed separately in 50 mM HEPES-NaOH (pH 7.5), 200 mM NaCl, 300 μM NaHCO$_3$ at 4°C overnight. MtsA was concentrated using an ultrafiltration unit (Amicon-Ultra-0.5, 10K, Merck KGaA, Darmstadt, Germany) and diluted with 50 mM HEPES-NaOH (pH 7.5), 200 mM NaCl, 300 μM NaHCO$_3$, and the process was repeated three times. The cell was filled with 10 μM antibodies, and the syringe was filled with 100 μM MtsA. The first injection of 0.5 μL (omitted from the analysis) was followed by 19 injections of 2 μL with 120 s intervals at a constant temperature of 25°C. The titration syringe was continuously stirred at 750 rpm. The obtained data were fitted by nonlinear regression of the integrated data to a one-site binding model using ORIGIN 7.0 software (MicroCal, Northampton, MA, USA).

4.11 | Circular dichroism spectra

Circular dichroism (CD) spectroscopy measurements were carried out using a JASCO J-820 spectropolarimeter (JASCO, Tokyo, Japan). For measurements in the far-ultraviolet region, each of the antibodies (10 μM, in 50 mM HEPES-NaOH (pH 7.5), 200 mM NaCl, 300 μM NaHCO$_3$) was placed in a 1-mm quartz cell and measured five times with a bandwidth of 1 nm. The molar ellipticity (Mol. Ellip. [deg cm^2 dmol^{-1}]) of each antibody was determined following Kelly et al. (2005)

$$\mathrm{Mol.\,Ellip.} = 100 \times \theta / (C \times d)$$

where θ is the observed ellipticity [°], C is the concentration of the protein [M], and d is the path length [cm].

4.12 | Differential scanning calorimetry

The thermal stability of the antibodies was measured by DSC using a MicroCal PEAQ-DSC Automated System (Malvern). The protein samples (1 mg/mL in 50 mM HEPES-NaOH (pH 7.5), 200 mM NaCl, 300 μM NaHCO$_3$) were heated from 20 to 110°C at a scanning rate of 1.0°C/min. The data were analyzed using MicroCal PEAQ-DSC software (Malvern).

4.13 | SEC with multi-angle light scattering detection

The MWs of complexes were determined using 10/300 Superdex 200 pg increase columns (Cytiva) with inline DAWN8+ MALS (Wyatt Technology, Santa Barbara, CA, USA), an ultraviolet detector (Shimadzu, Tokyo, Japan), and a refractive index detector (Shodex, New York, NY, USA). Protein samples (45 μL) were injected at 20 μM bpAb with 20 μM MtsA. Analysis was performed using ASTRA software (Wyatt Technology). The protein concentration was calculated from the refractive index. All detectors were calibrated using bovine serum albumin (Sigma-Aldrich, St. Louis, MO, USA).

4.14 | Negative stain electron microscopy and image processing

A mixture of 20 μM MtsA and 20 μM GS30 bpAb was loaded on a 10/300 Superdex 200 pg increase column pre-equilibrated with 50 mM HEPES-NaOH (pH 7.5) and 200 mM NaCl. The elution was fractionated and frozen in liquid nitrogen. Protein samples were thawed on ice and diluted to 100 nM. An aliquot of 3 μL of GS30 bpAb and MtsA complex were adsorbed for 30 s at room temperature to freshly glow-discharged carbon-coated 400 line/inch square mesh copper-grids (Gilder Grids, Lincolnshire, UK). Next, a 5 μL drop of 1%

phosphotungstic acid was applied on the grid for negative staining. Subsequently, the excess amount of solution was removed with a filter paper and the grid was stained with another drop of 1% phosphotungstic acid. The solution was removed and the grid was air-dried. Images were collected using a JEM-1400Plus TEM (JEOL, Tokyo, Japan) operated at 120 kV at a nominal magnification of 40k. The complete 149 ring-shaped particles were manually picked and classified into 50 classes by 2D classification using CryoSPARC (Punjani et al., 2017). Seventeen representative classes are shown in Figure 8e.

4.15 | Analytical SEC

Analytical SEC was conducted using a 10/300 Superdex 200 pg increase column and AKTA pure (Cytiva). Fifty millimolar HEPES-NaOH (pH 7.5), 200 mM NaCl, 300 μM NaHCO$_3$ was used as the running buffer, and the run was conducted at 4°C, flow 0.5 mL/min. For the analysis, bpAb and MtsA were mixed in a molar ratio of 1:1.2 and incubated at 4°C overnight. After 0.22 μm filtration, the sample was injected and the fraction of each complex was collected. The concentration was adjusted to 0.3 μM by dilution, and the solution was incubated at 4°C for several hours or 7 days. The same volume of samples were reinjected into the SEC column after filtration through a 0.22 μm filter.

4.16 | Metal binding analysis of MtsA by ITC

Managanase ion binding to MtsA without antibodies was measured using an iTC200 microcalorimeter as the control (Malvern). Manganese(II) chloride tetrahydrate (FUJIFILM Wako Pure Chemical Corporation, Richmond, VA, USA) was prepared at 500 mM in Milli-Q water and diluted to 200 μM with 50 mM HEPES-NaOH (pH 7.5), 200 mM NaCl, 300 μM NaHCO$_3$. MtsA was concentrated on an ultrafiltration unit (Amicon-Ultra-0.5, 10K, Merck KGaA) and diluted with 50 mM HEPES-NaOH (pH 7.5), 200 mM NaCl, 300 μM NaHCO$_3$, and the process was repeated three times. The cell was filled with 20 μM MtsA, and the syringe was filled with 200 μM freshly prepared manganese(II) chloride tetrahydrate. The first injection of 0.5 μL (omitted from the analysis) was followed by 19 injections of 2 μL with 120 s intervals at a constant temperature of 25°C. The titration syringe was continuously stirred at 750 rpm. The obtained data were fitted by nonlinear regression of the integrated data to a one-site binding model using ORIGIN 7.0 software.

The inhibition of metal binding by antibodies was also measured. To remove the metal ion within antibodies, the antibodies were dialyzed at 4°C overnight in 50 mM HEPES-NaOH (pH 7.5), 200 mM NaCl, 300 μM NaHCO$_3$ supplemented with 1 mM EDTA and subjected to SEC with a Hiload 26/60 Superdex 75 pg column equilibrated with 50 mM HEPES-NaOH (pH 7.5), 200 mM NaCl, 300 μM NaHCO$_3$. The eluted antibodies were dialyzed separately in 50 mM HEPES-NaOH (pH 7.5), 200 mM NaCl, 300 μM NaHCO$_3$ at 4°C overnight. The iTC200 cell was filled with 20 μM MtsA supplemented with 40 μM of antibodies, preliminarily incubated at room temperature for 30 min, and centrifuged at 4°C at 20,000 × g for 10 min to remove aggregations. The obtained data were analyzed using the program ORIGIN 7.0, and the binding of metal to MtsA was compared with the binding of metal to the complex of antibodies with MtsA.

ACCESSION NUMBERS
The final models of crystal structures were deposited to Protein Data Bank (PDB) as follows, Zn-bound MtsA PDB ID:8YJ6; scFv13-Zn-bound MtsA PDB ID:8YJ7; VHH43-bound MtsA PDB ID: 8YJ5; VHH43-Zn-bound MtsA PDB ID: 8YJ8.

AUTHOR CONTRIBUTIONS
Risa Asano: Conceptualization; data curation; investigation; writing – original draft. **Miyu Takeuchi:** Data curation; investigation; writing – review and editing. **Makoto Nakakido:** Conceptualization; investigation; supervision; funding acquisition; writing – original draft; project administration. **Sho Ito:** Methodology; software; investigation; writing – review and editing. **Chihiro Aikawa:** Investigation; data curation; writing – review and editing. **Takeshi Yokoyama:** Methodology; investigation; writing – review and editing; data curation. **Akinobu Senoo:** Data curation; investigation; writing – review and editing. **Go Ueno:** Methodology; writing – review and editing; data curation. **Satoru Nagatoishi:** Data curation; writing – review and editing; methodology. **Yoshikazu Tanaka:** Data curation; methodology; writing – review and editing. **Ichiro Nakagawa:** Writing – review and editing; supervision; investigation; data curation. **Kouhei Tsumoto:** Supervision; project administration; writing – review and editing; funding acquisition; conceptualization.

ORCID

Risa Asano https://orcid.org/0009-0007-7122-1221
Makoto Nakakido https://orcid.org/0000-0003-0328-9914
Akinobu Senoo https://orcid.org/0000-0001-6911-360X

REFERENCES

Adams PD, Afonine PV, Bunkóczi G, Chen VB, Davis IW, Echols N, et al. PHENIX: a comprehensive Python-based system for macromolecular structure solution. Acta Crystallogr D Biol Crystallogr. 2010;66:213–21.

Ahmad ZA, Yeap SK, Ali AM, Ho WY, Alitheen NBM, Hamid M. scFv antibody: principles and clinical application. Clin Dev Immunol. 2012;2012:980250.

Akiba H, Takayanagi K, Kusano-Arai O, Iwanari H, Hamakubo T, Tsumoto K. Generation of biparatopic antibody through two-step targeting of fragment antibodies on antigen using SpyTag and SpyCatcher. Biotechnol Rep (Amst). 2020;25:e00418.

Akiba H, Tsumoto K. Development and activities, including immunocomplex formation, of biparatopic antibodies and alternative scaffold proteins. Transl Regul Sci. 2020;2:1–6.

Asaadi Y, Jouneghani FF, Janani S, Rahbarizadeh F. A comprehensive comparison between camelid nanobodies and single chain variable fragments. Biomark Res. 2021;9:87.

Bannas P, Hambach J, Koch-Nolte F. Nanobodies and nanobody-based human heavy chain antibodies as antitumor therapeutics. Front Immunol. 2017;8:1603.

Bracken CJ, Lim SA, Solomon P, Rettko NJ, Nguyen DP, Zha BS, et al. Bi-paratopic and multivalent VH domains block ACE2 binding and neutralize SARS-CoV-2. Nat Chem Biol. 2021;17:113–21.

Brinkmann U, Kontermann RE. The making of bispecific antibodies. MAbs. 2017;9:182–212.

Brouwer S, Rivera-Hernandez T, Curren BF, Harbison-Price N, De Oliveira DMP, Jespersen MG, et al. Pathogenesis, epidemiology and control of group A Streptococcus infection. Nat Rev Microbiol. 2023;21:431–47.

Chen X, Zaro JL, Shen W-C. Fusion protein linkers: property, design and functionality. Adv Drug Deliv Rev. 2013;65:1357–69.

Couñago RM, Ween MP, Begg SL, Bajaj M, Zuegg J, O'Mara ML, et al. Imperfect coordination chemistry facilitates metal ion release in the Psa permease. Nat Chem Biol. 2014;10:35–41.

de Boer M, Gouridis G, Vietrov R, Begg SL, Schuurman-Wolters GK, Husada F, et al. Conformational and dynamic plasticity in substrate-binding proteins underlies selective transport in ABC importers. Elife. 2019;8:e44652. https://doi.org/10.7554/eLife.44652

Emmerson CD, van der Vlist EJ, Braam MR, Vanlandschoot P, Merchiers P, de Haard HJW, et al. Enhancement of polymeric immunoglobulin receptor transcytosis by biparatopic VHH. PLoS One. 2011;6:e26299.

Emsley P, Lohkamp B, Scott WG, Cowtan K. Features and development of coot. Acta Crystallogr D Biol Crystallogr. 2010;66:486–501.

Evers TH, van Dongen EMWM, Faesen AC, Meijer EW, Merkx M. Quantitative understanding of the energy transfer between fluorescent proteins connected via flexible peptide linkers. Biochemistry. 2006;45:13183–92.

Fan G, Wang Z, Hao M, Li J. Bispecific antibodies and their applications. J Hematol Oncol. 2015;8:130.

Fischer MJE. Amine coupling through EDC/NHS: a practical approach. Methods Mol Biol. 2010;627:55–73.

Ge R, Sun X. Iron acquisition and regulation systems in Streptococcus species. Metallomics. 2014;6:996–1003.

Glaven RH, Anderson GP, Zabetakis D, Liu JL, Long NC, Goldman ER. Linking single domain antibodies that recognize different epitopes on the same target. Biosensors. 2012;2:43–56.

Gräwe A, Ranglack J, Weyrich A, Stein V. iFLinkC: an iterative functional linker cloning strategy for the combinatorial assembly and recombination of linker peptides with functional domains. Nucleic Acids Res. 2020;48:e24.

Henry KA, MacKenzie CR. Antigen recognition by single-domain antibodies: structural latitudes and constraints. MAbs. 2018;10:815–26.

Henry KA, Nguyen T-D, Baral TN, Hussack G, Raphael S, Arbabi-Ghahroudi M, et al. Biparatopic single-domain antibodies against Axl achieve ultra-high affinity through intramolecular engagement. Biochem Biophys Res Commun. 2021;562:154–61.

Jakubovics NS. An ion for an iron: streptococcal metal homeostasis under oxidative stress. Biochem J. 2019;476:699–703.

Kabsch W. XDS. Acta Crystallogr D Biol Crystallogr. 2010;66:125–32.

Kaplon H, Crescioli S, Chenoweth A, Visweswaraiah J, Reichert JM. Antibodies to watch in 2023. MAbs. 2023;15:2153410.

Kawade R, Akiba H, Entzminger K, Maruyama T, Okumura CJ, Tsumoto K. Roles of the disulfide bond between the variable and the constant domains of rabbit immunoglobulin kappa chains in thermal stability and affinity. Protein Eng Des Sel. 2018;31:243–7.

Kelly SM, Jess TJ, Price NC. How to study proteins by circular dichroism. Biochim Biophys Acta. 2005;1751:119–39.

Labrijn AF, Janmaat ML, Reichert JM, Parren PWHI. Bispecific antibodies: a mechanistic review of the pipeline. Nat Rev Drug Discov. 2019;18:585–608.

Lei B, Liu M, Voyich JM, Prater CI, Kala SV, DeLeo FR, et al. Identification and characterization of HtsA, a second heme-binding protein made by Streptococcus pyogenes. Infect Immun. 2003;71:5962–9.

Lerchner A, Daake M, Jarasch A, Skerra A. Fusion of an alcohol dehydrogenase with an aminotransferase using a PAS linker to improve coupled enzymatic alcohol-to-amine conversion. Protein Eng Des Sel. 2016;29:557–62.

Lu D, Jimenez X, Zhang H, Bohlen P, Witte L, Zhu Z. Fab-scFv fusion protein: an efficient approach to production of bispecific antibody fragments. J Immunol Methods. 2002;267:213–26.

Ma J, Mo Y, Tang M, Shen J, Qi Y, Zhao W, et al. Bispecific antibodies: from research to clinical application. Front Immunol. 2021;12:626616.

Muyldermans S. Nanobodies: natural single-domain antibodies. Annu Rev Biochem. 2013;82:775–97.

Oganesyan V, Peng L, Bee JS, Li J, Perry SR, Comer F, et al. Structural insights into the mechanism of action of a biparatopic anti-HER2 antibody. J Biol Chem. 2018;293:8439–48.

Ohi M, Li Y, Cheng Y, Walz T. Negative staining and image classification – powerful tools in modern electron microscopy. Biol Proced Online. 2004;6:23–34.

Pekar L, Busch M, Valldorf B, Hinz SC, Toleikis L, Krah S, et al. Biophysical and biochemical characterization of a VHH-based IgG-like bi- and trispecific antibody platform. MAbs. 2020;12:1812210.

Pettersen EF, Goddard TD, Huang CC, Couch GS, Greenblatt DM, Meng EC, et al. UCSF Chimera—a visualization system for exploratory research and analysis. J Comput Chem. 2004;25:1605–12.

Potterton L, Agirre J, Ballard C, Cowtan K, Dodson E, Evans PR, et al. CCP4i2: the new graphical user interface to the CCP4 program suite. Acta Crystallogr D Struct Biol. 2018;74:68–84.

Punjani A, Rubinstein JL, Fleet DJ, Brubaker MA. cryoSPARC: algorithms for rapid unsupervised cryo-EM structure determination. Nat Methods. 2017;14:290–6.

Roovers RC, Vosjan MJWD, Laeremans T, el Khoulati R, de Bruin RCG, Ferguson KM, et al. A biparatopic anti-EGFR nanobody efficiently inhibits solid tumour growth. Int J Cancer. 2011;129:2013–24.

Schlapschy M, Binder U, Börger C, Theobald I, Wachinger K, Kisling S, et al. PASylation: a biological alternative to PEGylation for extending the plasma half-life of pharmaceutically active proteins. Protein Eng Des Sel. 2013;26:489–501.

Spiess C, Zhai Q, Carter PJ. Alternative molecular formats and therapeutic applications for bispecific antibodies. Mol Immunol. 2015;67:95–106.

Steinhardt JJ, Guenaga J, Turner HL, McKee K, Louder MK, O'Dell S, et al. Rational design of a trispecific antibody targeting the HIV-1 Env with elevated anti-viral activity. Nat Commun. 2018;9:877.

Sun X, Baker HM, Ge R, Sun H, He Q-Y, Baker EN. Crystal structure and metal binding properties of the lipoprotein MtsA, responsible for iron transport in Streptococcus pyogenes. Biochemistry. 2009;48:6184–90.

Sun X, Ge R, Chiu J-F, Sun H, He Q-Y. Lipoprotein MtsA of MtsABC in Streptococcus pyogenes primarily binds ferrous ion with bicarbonate as a synergistic anion. FEBS Lett. 2008;582:1351–4.

Turner AG, Djoko KY, Ong C-LY, Barnett TC, Walker MJ, McEwan AG. Group A Streptococcus co-ordinates manganese import and iron efflux in response to hydrogen peroxide stress. Biochem J. 2019;476:595–611.

Ueno G, Kanda H, Hirose R, Ida K, Kumasaka T, Yamamoto M. RIKEN structural genomics beamlines at the SPring-8; high throughput protein crystallography with automated beamline operation. J Struct Funct Genomics. 2006;7:15–22.

Wagner TR, Ostertag E, Kaiser PD, Gramlich M, Ruetalo N, Junker D, et al. NeutrobodyPlex-monitoring SARS-CoV-2 neutralizing immune responses using nanobodies. EMBO Rep. 2021;22:e52325.

Walter JD, Scherer M, Hutter CAJ, Garaeva AA, Zimmermann I, Wyss M, et al. Biparatopic sybodies neutralize SARS-CoV-2 variants of concern and mitigate drug resistance. EMBO Rep. 2022;23:e54199.

Yumura K, Akiba H, Nagatoishi S, Kusano-Arai O, Iwanari H, Hamakubo T, et al. Use of SpyTag/SpyCatcher to construct bispecific antibodies that target two epitopes of a single antigen. J Biochem. 2017;162:203–10.

SUPPORTING INFORMATION

Additional supporting information can be found online in the Supporting Information section at the end of this article.